CCD Photometry, Period Study, and Light Curve Modeling of the Overcontact Binary Systems NSVS 5374825 and GR Piscium

Kevin B. Alton
UnderOak Observatory, 70 Summit Avenue, Cedar Knolls, NJ 07927; kbalton@optonline.net

Received May 4, 2022; revised June 30, 2022; accepted July 5, 2022

Abstract During this study precise time-series multi-bandpass (B, V, and I_c) light curve (LC) data for NSVS 5374825 (2018–2019) and GR Psc (2019) were acquired at Desert Blooms Observatory (DBO). Both targets produced new times of minimum which were used along with other eclipse timings mined from the SuperWASP survey and the literature to update their corresponding ephemerides. Preliminary evidence suggests a secular decrease in the orbital period of GR Psc between 2004 and 2019, while during the same time span NSVS 5374825 experienced an increase in its orbital period. Roche modeling to produce synthetic fits to the observed LC data was accomplished using the Wilson-Devinney code. Since each system exhibits a total eclipse, a reliable value for the mass ratio (q) could be determined leading in turn to initial estimates for the physical and geometric elements of both variable systems. Absolute determinations will still require radial velocity and high resolution spectral classification studies.

1. Introduction

CCD-derived photometric data for NSVS 5374825 (GSC 3111-0679) were first acquired from the ROTSE-I survey between 1999–2000 (Akerlof *et al.* 2000; Woźniak *et al.* 2004; Gettel *et al.* 2006) and later from the Catalina Sky (Drake *et al.* 2014), SuperWASP (Butters *et al.* 2010), and ASAS-SN (Jayasinghe *et al.* 2018) surveys. Its classification as a W UMa variable was assigned according to Hoffman *et al.* (2009). No other times of minimum (ToM) have been found in the literature; this paper marks the first detailed period analysis and multi-color Roche model assessment of light curves (LCs) for NSVS 5374825. In a similar fashion the variability of GR Psc (GSC 1747-0967) was initially observed (Martignoni 2006) from data acquired during the ROTSE-1 Survey (1999–2000). Later on (2005–2013) sparsely-sampled light curve data were collected during the Catalina Sky Survey, ASAS (Pojmański 2005), SuperWASP (Butters *et al.* 2010), and ASAS-SN (Jayasinghe *et al.* 2018) surveys. Michaels (2020) published a detailed investigation on GR Psc which coincidently included photometric data (B,V, g', r') acquired during nearly the same time period (October–November 2019) as the study herein. With one notable exception, the results from both studies were very similar.

2. Observations and data reduction

Precise time-series photometric observations were acquired at Desert Blooms Observatory (DBO, USA: 31.941 N, 110.257 W) using two different CCD cameras. In 2018, NSVS 5374825 images were obtained with an SBIG STT-1603ME CCD camera mounted at the Cassegrain focus of a 0.4-m Schmidt-Cassegrain telescope. This combination (f/6.8) produced an image scale of 1.36 arcsec/pixel (bin = 2 × 2) and a field-of-view (FOV) of 11.5' × 17.2'. In 2019 all photometric data were generated using a QSI 683 wsg-8 CCD camera mounted on the same optical tube assembly. This focal-reduced (f/7.2) instrument produced an image scale of 0.76 arcsec/pixel (bin = 2 × 2) and a field-of-view (FOV) of 15.9 × 21.1 arcmin. In both cases the CCD cameras were equipped with photometric B, V, and I_c filters manufactured to match the Johnson-Cousins Bessell specification. Image (science, darks, and flats) acquisition software (TheSkyX Pro Edition 10.5.0; Software Bisque 2019) controlled the main and off-axis guide cameras. Computer clock time was updated immediately prior to each session. Dark subtraction, flat correction, and registration of all images collected at DBO were performed with AIP4Win v2.4.1 (Berry and Burnell 2005). Instrumental readings were reduced to catalog-based magnitudes using the APASS star fields (Henden *et al.* 2009, 2010, 2011; Smith *et al.* 2011) built into MPO Canopus v10.7.1.3 (Minor Planet Obs. 2010). In order to minimize any potential error due to differential refraction and color extinction, only data from images taken above 30° altitude (airmass <2.0) were included. All photometric data acquired from NSVS 5374825 and GR Psc at DBO can be retrieved from the AAVSO International Database (Kafka 2021; observer code "AKV").

Uncertainty in comparison star measurements made in the same FOV with NSVS 5374825 or GR Psc typically stayed within ± 0.007 mag for V- and I_c- and ± 0.010 mag for B-passbands. The identity, J2000 coordinates, and color indices (B–V) for these stars are provided in Table 1. AAVSO finder charts for NSVS 5374825 (Figure 1) and GR Psc (Figure 2) are centered around each target along with its corresponding ensemble (1–5) of comparison stars.

3. Results and discussion

Results and detailed discussion about the determination of linear and quadratic ephemerides are provided in this section. Thereafter, the multi-source approach for estimating the effective temperatures for NSVS 5374825 and GR Psc along with Roche-lobe modeling results with the W-D code are examined. Finally, preliminary estimates for mass ($M_\odot$) and radius ($R_\odot$), along with corresponding calculations for luminosity ($L_\odot$), surface gravity (log (g)), semi-major axis ($R_\odot$), and bolometric magnitude (M_{bol}), are derived.

Table 1. Astrometric coordinates (J2000), V-mags and color indices (B - V) for NSVS 5374825, GR Psc, and their corresponding five comparison stars used in this photometric study.

Star	*R.A.* h m s	*Dec.* ° ′ ″	*V-mag*[a]	*(B−V)*[a]
NSVS 5374825	18 10 33.53	+42 16 23.1	13.228	0.586
GSC 3111-1428	18 10 18.31	+42 15 49.2	13.227	0.796
GSC 3110-1324	18 09 18.73	+42 13 21.1	12.836	0.857
GSC 3110-1053	18 09 37.61	+42 12 55.1	14.084	0.559
GSC 3111-1679	18 10 06.28	+42 09 32.7	14.094	0.553
GSC 3111-1650	18 10 14.35	+42 12 22.9	14.048	0.460
GR Psc	01 09 31.89	+22 39 19.8	11.296	0.444
GSC 1747-0927	01 06 38.53	+22 46 22.8	11.355	1.117
GSC 1747-0179	01 09 15.13	+22 44 17.4	12.109	0.603
GSC 1747-0517	01 10 21.93	+22 51 59.1	10.916	0.502
GSC 1747-0623	01 10 18.66	+22 38 02.6	12.469	0.663
GSC 1747-0841	01 10 20.39	+22 37 24.9	13.172	0.593

[a] *V-mag and (B−V) for comparison stars derived from APASS database described by Henden* et al. *(2009, 2010, 2011) and Smith* et al. *(2011).*

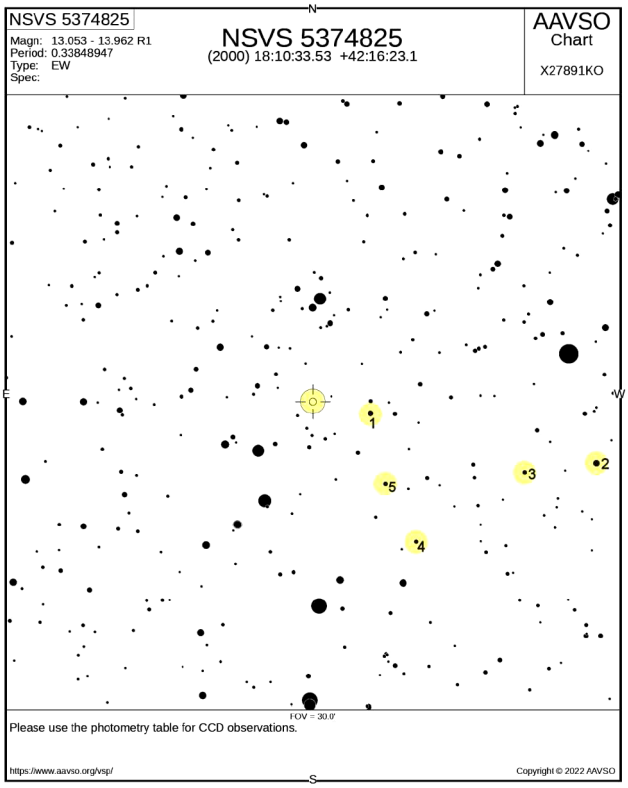

Figure 1. Finder chart for NSVS 5374825 (center) also showing the comparison stars (1–5) used for aperture-derived ensemble photometry.

3.1. Photometry and ephemerides

ToM values and associated errors from data acquired at DBO were calculated according to Andrych and Andronov (2019) and Andrych *et al.* (2020) using the program MAVKA (https://uavso.org.ua/mavka/). Simulation of extrema (Min I and Min II) was automatically optimized by finding the most precise degree (α) and best fit algebraic polynomial expression. A "wall-supported line" (WSL) algorithm (Andrych *et al.* 2017) provided the best fit, as the eclipse passes through totality, resulting in a flattened bottom. Long-term or secular changes in orbital

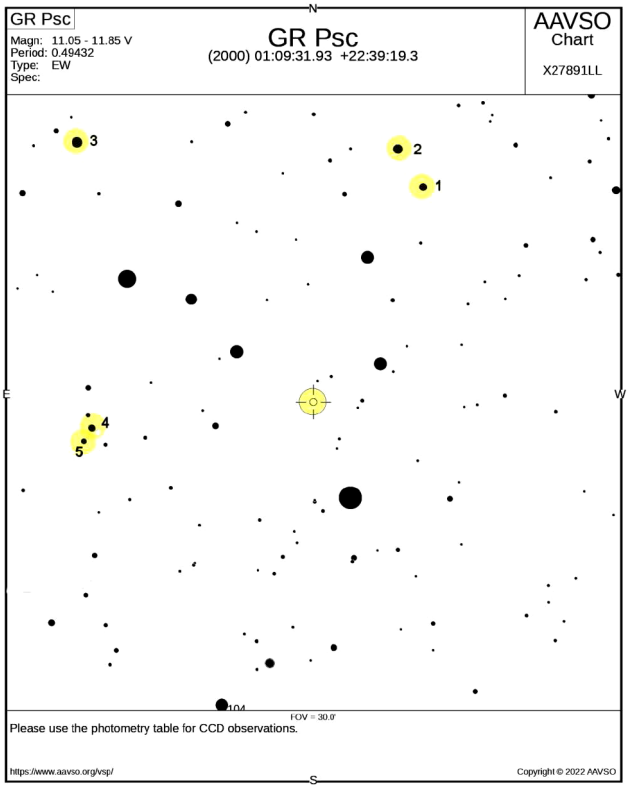

Figure 2. Finder chart for GR Psc (center) also showing the comparison stars (1–5) used for aperture-derived ensemble photometry.

period can sometimes be revealed by plotting the difference between the observed eclipse times and those predicted by a reference epoch against cycle number. These residuals (ETD) vs. epoch were fit using scaled Levenberg-Marquardt algorithms (QtiPlot ~0.9.9–rc9; https://www.qtiplot.com/). The results from these analyses are separately discussed for each binary system in the subsections below. NSVS 5374825 and GR Psc were also imaged during the SuperWASP survey (Butters *et al.* 2010), which provided a rich source of photometric data taken (30-s exposures) at modest cadence that repeats every 9 to 12 min. In some cases (NSVS 5374825, n = 80; GR Psc, n = 36) SuperWASP measurements taken between 2004 and 2008 were amenable to extrema estimation using MAVKA.

3.1.1. NSVS 5374825

A total of 584 photometric values in B-, 589 in V-, and 571 in I_c-passbands were acquired at DBO from NSVS 5374825 between 19 May 2018 and 27 May 2019. Included in these determinations were nine new times of minimum (ToM) acquired during this study which are summarized in Table 2. Period-folded LCs from the Catalina Sky and ASAS-SN surveys were used to interpolate a mid-point time during Min I and Min II. These two results, along with other eighty ToM values estimated from the SuperWASP survey from 2004 through 2008, were used to determine whether any secular changes in the orbital period could be detected from the eclipse timing residuals.

Inspection of the ETD residuals vs. epoch plot (Figure 3) reveals a parabolic relationship. ToM values acquired between 2017 and 2019 were used to determine a near-term linear ephemeris:

Table 2. Sample table of NSVS 5374825 times-of-minimum (16 May 2004–27 May 2019), cycle number and eclipse timing difference (ETD) between observed and predicted times derived from the updated linear ephemeris (Equation 1).

HJD = 2400000+	*HJD Error*	*Cycle No.*	*ETD*	*Ref.*
53141.6420	0.0002	–16216.5	0.0315	1
53142.6588	0.0007	–16213.5	0.0328	1
53143.6711	0.0003	–16210.5	0.0296	1
54621.5160	0.0003	–11844.5	0.0179	1
54623.5476	0.0002	–11838.5	0.0185	1
54624.5629	0.0006	–11835.5	0.0183	1

References in sample: (1) SuperWASP (Butters et al. 2010); Full table available at: ftp://ftp.aavso.org/public/datasets/3831-Alton-NSVS_5374825.txt. All references relevant to the full table that appears on the AAVSO ftp site are included in the References section of this article. All references are given in the full table.

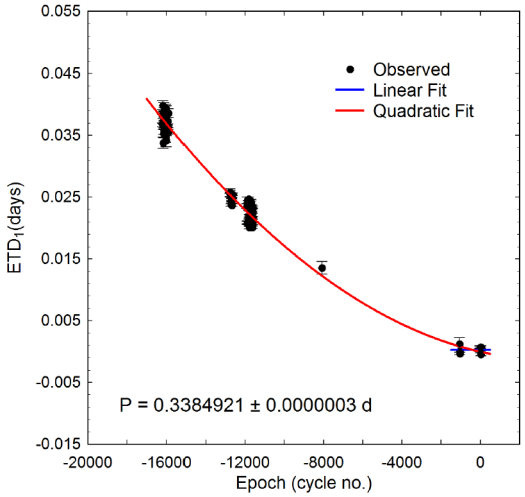

Figure 3. The upwardly directed quadratic fit (Equation 2) to the ETD vs. epoch data is shown with a solid red line and suggests the orbital period of NSVS 5374825 is increasing with time. The linear ephemeris (Equation 1) was determined from near-term data acquired between 2017 and 2019 (solid blue line). ToM measurement uncertainty is defined by the error bars.

Table 3. Sample table of GR Psc times-of-minimum (13 July 2004–20 Nov 2019), cycle number and eclipse timing difference (ETD) between observed and predicted times derived from the updated linear ephemeris (Equation 3).

HJD = 2400000+	*HJD Error*	*Cycle No.*	*ETD*	*Ref.*
53199.6707	0.0003	–11344.5	–0.0082	1
53200.6585	0.0004	–11342.5	–0.0090	1
53201.6472	0.0004	–11340.5	–0.0089	1
54020.4896	0.0003	–9684	–0.0057	1
54021.4782	0.0005	–9682	–0.0058	1
54022.4674	0.0003	–9680	–0.0052	1

[a] Outlier value not included in period analyses; nr = not reported ("a" and "nr" not shown in this sample).
References in sample: (1) SuperWASP (Butters et al. 2010); Full table available at: ftp://ftp.aavso.org/public/datasets/3831-Alton-GR_Psc.txt. All references relevant to the full table that appears on the AAVSO ftp site are included in the References section of this article. All references are given in the full table.

$$\text{Min. I (HJD)} = 2458630.76818(3) + 0.3384921(3)\,E. \quad (1)$$

The difference between the observed eclipse times and those predicted by the linear ephemeris (Equation 1) against epoch (cycle number) was best fit by a quadratic relationship (Equation 2) where:

$$ETD = -2.2799 \cdot 10^{-4} - 2.8854 \cdot 10^{-7}\,E + 9.9473 \cdot 10^{-11}\,E^2. \quad (2)$$

Since the coefficient of the quadratic term (Q) is positive, this result would suggest that the orbital period has been increasing at a constant rate ($dP/dt = 2Q/P$) of 0.0185 ± 0.0011 s · y^{-1}. This rate is similar to many other overcontact systems reported in the literature (Latković *et al.* 2021). Period change over time that can be described by a parabolic expression is often attributed to mass transfer or by angular momentum loss (AML) due to magnetic stellar wind (Qian 2001, 2003; Li *et al.* 2019). Ideally, when AML dominates, the net effect is a decreasing orbital period. If conservative mass transfer from the more massive to its less massive secondary star prevails, then the orbital period can also decrease. Separation increases when conservative mass transfer from the less massive to its more massive binary cohort takes place or spherically symmetric mass loss from either body (e.g. a wind but not magnetized) occurs. In mixed situations (e.g. mass transfer from less massive star, together with AML) the orbit evolution depends on which process dominates. Since the orbital period is not a constant, then linear ephemerides need to be regularly updated.

3.1.2. GR Psc

A total of 733 photometric values in B-, 690 in V-, and 703 in I_c-passbands were acquired from GR Psc between October 19, 2019, and November 15, 2019. Included in these determinations were seven new ToM values acquired at DBO which are provided in Table 3. Twenty-one ToM estimates from the literature, along with thirty-six ToM values determined from the SuperWASP survey from 2004 through 2008, were used to determine whether any secular changes in the orbital period could be detected from the eclipse timing residuals. An updated linear ephemeris (Equation 3) based on near term ETD values (2012–2019) was derived as follows:

$$\text{Min. I (HJD)} = 2458807.47917(7) + 0.4943189(1)\,E. \quad (3)$$

These data are shown as a blue horizontal line in Figure 4. Nevertheless, since the orbital period appears to be decreasing at a constant rate, ephemerides for GR Psc will need to be updated on a regular basis.

Plotting the difference between the observed eclipse times and those predicted by the linear ephemeris against epoch (Figure 4) uncovered what appears to be a quadratic relationship (Equation 4) where:

$$ETD = -6.5912 \cdot 10^{-5} - 3.8752 \cdot 10^{-7}\,E - 9.8507 \cdot 10^{-11}\,E^2. \quad (4)$$

In this case the ETD residuals vs. epoch can be best described by an expression with a negative quadratic coefficient ($-9.8507 \cdot 10^{-11}$), suggesting that the orbital period has been slowly decreasing

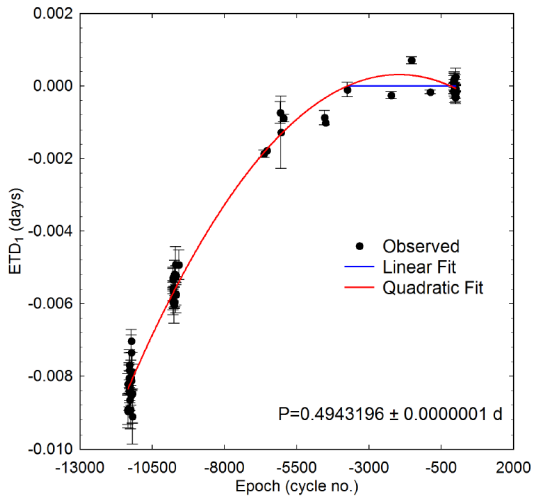

Figure 4. The downwardly directed quadratic fit to the ETD vs. epoch data (Equation 4) is shown with a solid red line and suggests the orbital period of GR Psc is decreasing with time. The linear ephemeris (Equation 3) (solid blue line) is determined from near-term data acquired between 2014 and 2019. Measurement uncertainty is defined by the error bars when available.

over time at the rate of $-0.0126\,(6)\,s \cdot y^{-1}$. Michaels (2020) reported a more rapid orbital period change rate ($-0.021\,s \cdot y^{-1}$). These differences are largely attributed to the inclusion of additional ToM values from the SuperWASP survey as well as those acquired at DBO. Nonetheless, both values are consistent with many other overcontact systems reported in the literature (Latković *et al.* 2021).

3.2. Effective temperature estimation

Throughout this paper the primary star is defined as the more massive member of each binary system. No medium-to-high resolution classification spectra were found in the literature for either variable. Therefore, the effective temperature (T_{eff1}) of each primary star has been estimated using color index (B–V) data acquired at DBO and others determined from astrometric (USNO-A2.0, USNO-B1.0, and UCAC4) and photometric (2MASS and APASS) surveys. These were transformed as necessary to (B–V)[1,2]. Interstellar extinction (A_V) was calculated ($E(B–V) \times 3.1$) using the reddening value (E(B–V)) estimated from Galactic dust map models reported by Schlafly and Finkbeiner (2011).

The intrinsic color ($(B–V)_0$) for NSVS 5374825 that was calculated from measurements made at DBO and those acquired from three other sources are listed in Table 4. Additional temperature values were mined from the Gaia DR2[3] (Gaia Collaboration *et al.* 2016, 2018), LAMOST DR5[4], and TESS[5] websites. The median T_{eff} and median absolute deviation values derived from all sources indicate a primary star with an effective temperature (5400 ± 173 K) that probably ranges in spectral class between G7V and K1V. These values represent a fairly broad range of temperatures (840 K) in which uncertainty of the mean (5550) approaches ±400 K. The potential impact on parameter estimates from Roche modeling with the WD code is addressed in section 3.4.

Similarly, dereddened color indices ($(B–V)_0$) for GR Psc gathered from different sources are listed in Table 5. The median value (6700 ± 200 K) adopted for Roche modeling corresponds to a primary star that likely ranges in spectral class between F1V and F5V.

3.3. Modeling approach with Wilson-Devinney code

Roche modeling of LC data from NSVS 5374825 (Figure 5) and GR Psc (Figure 6) was accomplished using the programs

Table 4. Derivation of the primary star effective temperature (Teff1) of NSVS 5374825 based upon temperature estimates from multiple sources.

	APASS	*USNO-A2.0*	*2MASS*	*Present Study*	*Gaia DR2*[a]	*LAMOST DR5*[b]	*TESS*[c]	*Houdashelt* et al. *(2000)*
$(B-V)_0$[d]	0.540	0.844	0.744	0.551	—	—	—	—
T_{eff}[e] (K)	6100	5180	5464	6045	5260^{+188}_{-246}	5322 (29)	5299 (231)	5733 (263)
Spectral Class[f]	F8V-F9V	K0V-K1V	G8V-G9V	F8V-F9V	K0V-K1V	G9V-K0V	G9V-K0V	G2V-G3V

[a] *Gaia Collab. (2016, 2018).* [b] *Zhao* et al. *(2012); Wang* et al. *(2019).* [c] *https://exofop.ipac.caltech.edu/tess/ .* [d] *Intrinsic $(B-V)_0$ determined using reddening value $E(B-V) = 0.0459 \pm 0.0019$; T_{eff1} interpolated from Pecaut and Mamajek (2013).* [e] *Median of all T_{eff1} values (5400 ± 173 K) adopted for LC modeling which most likely corresponds to a G7V-K1V main sequence star.* [f] *Spectral class range estimated from Pecaut and Mamajek (2013).*

Table 5. Derivation of the primary star eective temperature (Teff1) of GR Psc based upon temperature estimates from multiple sources.

	APASS	*USNO-A2.0*	*2MASS*	*Present Study*	*Terrell* et al. *(2012)*	*Gaia DR2*[a]	*TESS*[b]	*Houdashelt* et al. *(2000)*
$(B-V)_0$[c]	0.404	0.469	0.374	0.423	0.365	—	—	—
T_{eff1}[d] (K)	6669	6396	6812	6586	6861	6909^{+285}_{-232}	6790 (361)	6570 (200)
Spectral Class[e]	F3V-F4V	F5V-F6V	F1V-F2V	F1V-F2V	F1V-F2V	F1V-F2V	F2V-F3V	F4V-F5V

[a] *Gaia Collab. (2016, 2018).* [b] *https://exofop.ipac.caltech.edu/tess/ .* [c] *Intrinsic $(B-V)_0$ determined using reddening value $E(B-V) = 0.0392 \pm 0.0005$; T_{eff1} interpolated from Pecaut and Mamajek (2013).* [d] *Median of all T_{eff1} values (6700 ± 200 K) adopted for LC modeling which most likely corresponds to a F1V-F5V main sequence star.* [e] *Spectral class range estimated from Pecaut and Mamajek (2013).*

[1] http://www.aerith.net/astro/color_conversion.html
[2] http://brucegary.net/dummies/method0.html
[3] http://vizier.u-strasbg.fr/viz-bin/VizieR?-source=I/345/gaia2
[4] http://dr5.lamost.org/search [5] https://exofop.ipac.caltech.edu/tess/

PHOEBE 0.31a (Prša and Zwitter 2005) and WDwint56a (Nelson 2009). Both feature a user friendly GUI interface to the Wilson-Devinney WD2003 code (Wilson and Devinney 1971; Wilson 1979; 1990). WDwint56a makes use of Kurucz's atmosphere models (Kurucz 2002), which are integrated over BVR_cI_c optical passbands. In both cases, the selected model was Mode 3 for an overcontact binary. Other modes (detached and semi-detached) were explored but never approached the goodness of fit achieved with Mode 3. Since the internal energy transfer to the surface of both variable systems is driven by convective (T_{eff1} <7500 K) rather than radiative processes, the bolometric albedo ($A_{1,2}$ = 0.5) was assigned according to Ruciński (1969) while the gravity darkening coefficient ($g_{1,2}$ = 0.32) was adopted from Lucy (1967). Logarithmic limb darkening coefficients (x_1, x_2, y_1, y_2) were interpolated (Van Hamme 1993) following each change in the effective temperature (T_{eff2}) of the secondary star during model fit optimization using differential corrections (DC). All but the temperature of the more massive star (T_{eff1}), $A_{1,2}$, and $g_{1,2}$ were allowed to vary during DC iterations. In general, the best fits for T_{eff2}, i, q, and Roche potentials ($\Omega_1 = \Omega_2$) were collectively refined (method of multiple subsets) by DC using the multicolor LC data. LCs from NSVS 5374825 (Figure 5) and GR Psc (Figure 6) do not exhibit significant asymmetry during quadrature (Max I ≅ Max II), which is often called the O'Connell effect (O'Connell 1951). As such, no spot was invoked to improve LC simulations for either variable. Third-light contribution (l_3) during DC optimization did not lead to any value significantly different from zero with either binary system. A detailed discussion of the determined mass ratio and derived masses follows in subsequent sections.

3.4. Modeling results with Wilson-Devinney code

It is generally not possible to determine unambiguously the mass ratio or total mass of an eclipsing binary system without spectroscopic radial velocity (RV) data. Standard errors reported in Tables 6 and 7 are computed from the DC covariance matrix and only reflect the model fit to the observations which assume exact values for any fixed parameter. These formal errors are generally regarded as unrealistically small considering the estimated uncertainties associated with the mean adopted T_{eff1} values along with basic assumptions about $A_{1,2}$, $g_{1,2}$, and the influence of spots added to the WD model. Normally, values for T_{eff1}, $A_{1,2}$, and $g_{1,2}$ are fixed with no error during modeling with the WD code. When T_{eff1} is varied by as much as ±10%, investigations with other OCBs including A- (Alton 2019; Alton *et al.* 2020) and W-subtypes (Alton and Nelson 2018) have shown that uncertainty estimates for i, q, or $\Omega_{1,2}$ were not appreciably (<2.5%) affected. Assuming that the actual T_{eff1} value falls within ±10% of the adopted values used for WD modeling (a reasonable expectation based on T_{eff1} data provided in Tables 4 and 5), then uncertainty estimates for i, q, or $\Omega_{1,2}$ would likely not exceed this amount.

The fill-out parameter (f) which corresponds to the outer surface shared by each star was calculated according to Equation 5 (Kallrath and Milone 1999; Bradstreet 2005) where:

$$f = (\Omega_{inner} - \Omega_{1,2}) / (\Omega_{inner} - \Omega_{outer}), \quad (5)$$

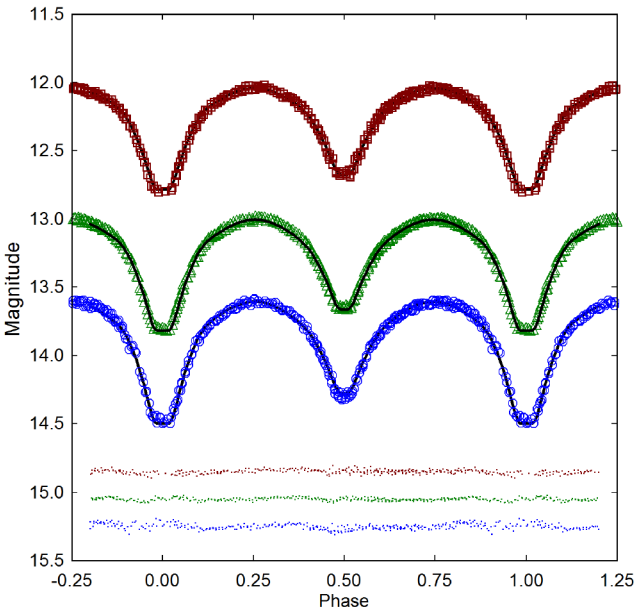

Figure 5. Folded CCD light curves for NSVS 5374825 produced from photometric data obtained between May 15, 2019, and May 27, 2019. The top (I_c), middle (V), and bottom curves (B) shown above were reduced to APASS-based catalog magnitudes using MPO Canopus. In this case, the Roche model (solid black lines) assumed a W-type overcontact binary with no spots; residuals from the model fits are offset at the bottom of the plot to keep the values on scale.

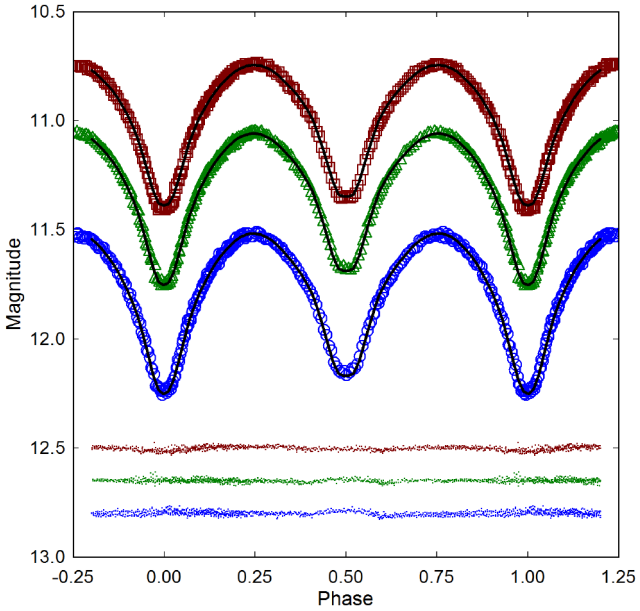

Figure 6. Folded CCD light curves for GR Psc produced from photometric data obtained between October 19, 2019, and November 15, 2019. The top (I_c), middle (V) and bottom curve (B) shown above were reduced to APASS-based catalog magnitudes using MPO Canopus. In this case, the Roche model (solid black lines) assumed an A-type overcontact binary with no spots; residuals from the model fits are offset at the bottom of the plot to keep the values on scale.

Ω_{outer} is the outer critical Roche equipotential, Ω_{inner} is the value for the inner critical Roche equipotential, and $\Omega = \Omega_{1,2}$ denotes the common envelope surface potential for the binary system. In both cases the systems are considered overcontact since 0 < f < 1.

3.4.1. NSVS 5374825

Only photometric data (BVI_c) acquired during 2019 were modeled using the Wilson-Devinney code (Figure 5). Derived

LC parameters and geometric elements are summarized in Table 6. In the case of NSVS 5374825 the flattened bottom at Min I (Figure 7) is indicative of a total eclipse, thereby suggesting that this system is a W-subtype overcontact binary system (Binnendijk 1970). Consequently, WD modeling proceeded under this assumption. With totality, degeneracy between the radii and inclination is broken (Terrell and Wilson 2005; Terrell 2022) such that a mass ratio can be determined with very small (<1%) relative error (Liu 2021). The Roche model for NSVS 5374825 did not require the addition of a spot or third light to improve the LC fits. Spatial images rendered (Figure 8) using Binary Maker 3 (BM3: Bradstreet and Steelman 2004) illustrate transit of the secondary across the primary face during Min II ($\varphi = 0.5$) and the shallow contact ($f = 0.11$) between each star.

3.4.2. GR Psc

The flattened bottom (Figure 7) observed during Min II is a diagnostic indicator for a total eclipse of the secondary star. It follows that the deepest minimum light (Min I) occurs when the smaller secondary transits the primary star (Figure 9). In this regard GR Psc behaves like an A-type overcontact binary and was therefore modeled accordingly. The Roche model for GR Psc did not require the addition of a spot or third light to improve the LC fits. LC parameters and geometric elements derived from the WD code are summarized in Table 7. Spatial renderings produced using BM3 (Figure 9) show (bottom) transit of the secondary during Min I ($\varphi = 0$) and the moderate contact ($f = 0.43$) between the two stars.

Except for a hot spot in the neck region of the primary star (Michaels 2020), a comparison of best fit results (Table 7) from both studies reveals very little difference in all other Roche model parameter estimates. Positioning a hot spot in the same region using data acquired at DBO during the same time period (2019) did not improve the fit in any bandpass (BVI_c). Perhaps the adopted higher effective temperature (6811 vs. 6700 K) and the different bandpasses (BVg'r' vs. BVI_c) account for this disparity.

3.5. Stellar parameters

Fundamental stellar parameters were estimated for both binary stars using results from the 2019 LC simulations. Importantly, without supporting RV data and classification spectra, these results should be considered preliminary and would be more accurately described as "relative" rather than "absolute."

3.5.1. NSVS 5374825

Calculations are described below for estimating the solar mass and size, semi-major axis, solar luminosity, bolometric V-mag, and surface gravity of each component (Table 8). Four empirically derived mass-period relationships (M-PR) for W UMa-binaries were used to estimate the primary star mass. The first M-PR was reported by Qian (2003), others followed from Gazeas and Stępień (2008), Gazeas (2009), and more recently Latković *et al.* (2021). According to Qian (2003), when the primary star is less than 1.35 $M_\odot$ or the system is W-type, its mass can be determined from:

Table 6. Lightcurve parameters evaluated by Roche modeling and the geometric elements derived for NSVS 5374825 assuming it is a W-type WUMa variable with no spots.

Parameter	*No spot*
T_{eff1} (K)[a]	5400 (173)
T_{eff2} (K)	5797 (186)
q (m_2 / m_1)	0.486 (1)
A[a]	0.5
g[a]	0.32
$\Omega_1 = \Omega_2$	2.816 (3)
i °	89.6 (4)
$L_1 / (L_1 + L_2)B$[b]	0.5535 (4)
$L_1 / (L_1 + L_2)V$	0.5811 (2)
$L_1 / (L_1 + L_2)I_c$	0.6029 (3)
r_1 (pole)	0.4222 (4)
r_1 (side)	0.4499 (5)
r_1 (back)	0.4800 (6)
r_2 (pole)	0.3033 (11)
r_2 (side)	0.3174 (13)
r_2 (back)	0.3537 (23)
Fill-out factor (%)	11
RMS (B)[c]	0.01317
RMS (V)[c]	0.00786
RMS (I_c)[c]	0.01048

All error estimates for T_{eff2}, q, $\Omega_{1,2}$, i, $r_{1,2}$, and L_1 from WDwint56A (Nelson 2009). [a] Fixed during DC. [b] L_1 and L_2 refer to scaled luminosities of the primary and secondary stars, respectively. [c] Monochromatic residual mean square error from observed values.

Table 7. Lightcurve parameters evaluated by Roche modeling and the geometric elements derived for GR Psc assuming it is an A-type W UMa variable with no spots.

Parameter	*This Study*	*Michaels 2020*
T_{eff1} (K)[a]	6700 (200)	6811
T_{eff2} (K)	6665 (199)	6760 (4)
q (m_2 / m_1)	0.432 (1)	0.431 (6)
A[a]	0.5	0.5
g[a]	0.32	0.32
$\Omega_1 = \Omega_2$	2.632 (1)	.619 (9)
i °	84.14 (11)	83.9 (3)
$A_S = T_S / T_{[star]}$[b]	—	1.06 (2)
Θ_S(spot co-latitude)[b]	—	98 (5)
φ_S (spot longitude)[b]	—	4 (2)
r_S (angular radius)[b]	—	19 (2)
$L_1 / (L_1 + L_2)B$[c]	0.6795 (1)	0.682 (10)
$L_1 / (L_1 + L_2)V$	0.6783 (1)	0.680 (10)
$L_1 / (L_1 + L_2)I_c$	0.6770 (1)	—
r_1 (pole)	0.4470 (2)	—
r_1 (side)	0.4817 (3)	0.4814 (8)
r_1 (back)	0.5178 (3)	—
r_2 (pole)	0.3103 (6)	—
r_2 (side)	0.3272 (7)	0.3452 (61)
r_2 (back)	0.3787 (16)	—
Fill-out factor (%)	43	47
RMS (B)[d]	0.00729	—
RMS (V)[d]	0.00562	—
RMS (I_c)[d]	0.00638	—

All error estimates for T_{eff2}, q, i, $\Omega_{1,2}$, A_S, Θ_S, φ_S, r_S, $r_{1,2}$, and L_1 from WDwint56A (Nelson 2009). [a] Fixed during DC. [b] Temperature factor (A_S); location (Θ_S, φ_S) and size (r_S) parameters in degrees. [c] L_1 and L_2 refer to scaled luminosities of the primary and secondary stars, respectively. [d] Monochromatic residual mean square fit from observed values.

$$M_1 = 0.391(59) + 1.96(17) \cdot P, \quad (6)$$

or alternatively when $M_1 > 1.35\,M_\odot$ or A-type then Equation 7:

$$M_1 = 0.761(150) + 1.82(28) \cdot P, \quad (7)$$

where P is the orbital period in days. Equation 6 leads to $M_1 = 1.05 \pm 0.08\,M_\odot$ for the primary.

The M-PR derived by Gazeas and Stępień (2008):

$$\log(M_1) = 0.755(59) \cdot \log(P) + 0.416(24), \quad (8)$$

corresponds to an OCB system where $M_1 = 1.15 \pm 0.10\,M_\odot$.

Gazeas (2009) reported another empirical relationship for the more massive (M_1) star of a contact binary such that:

$$\log(M_1) = 0.725(59) \cdot \log(P) - 0.076(32) \cdot \log(q) + 0.365(32). \quad (9)$$

from which $M_1 = 1.12 \pm 0.075\,M_\odot$.

Finally, Latković *et al.* (2021) conducted an exhaustive analysis from nearly 700 W UMa stars in which they established mass-period, radius-period, and luminosity-period relationships for the primary and secondary stars. Accordingly, the M-PR:

$$M_1 = (2.94 \pm 0.21 \cdot P) + (0.16 \pm 0.08). \quad (10)$$

leads to a primary star mass of $1.16 \pm 0.11\,M_\odot$. Using the photometric mass ratio ($q_{ptm} = 0.486 \pm 0.001$) derived from the LC model, the mean from these four values ($M_1 = 1.12 \pm 0.05\,M_\odot$) led to subsequent determinations of the secondary mass ($0.54 \pm 0.02\,M_\odot$) and total mass ($1.65 \pm 0.05\,M_\odot$).

The semi-major axis, $a(R_\odot) = 2.42 \pm 0.02$, was calculated from Newton's version of Kepler's third law where:

$$a^3 = (G \cdot P^2 (M_1 + M_2)) / (4\pi^2). \quad (11)$$

The effective radius of each Roche lobe (r_L) can be calculated over the entire range of mass ratios ($0 < q < \infty$) according to an expression derived by Eggleton (1983):

$$r_L = (0.49q^{2/3}) / (0.6q^{2/3} + \ln(1 + q^{1/3})), \quad (12)$$

from which values for r_1 (0.4425 ± 0.0003) and r_2 (0.3185 ± 0.0002) were determined for the primary and secondary stars, respectively. The radii in solar units for both binary components can be calculated such that $R_1 = a \cdot r_1 = 1.07 \pm 0.01\,R_\odot$ and $R_2 = a \cdot r_2 = 0.77 \pm 0.01\,R_\odot$.

Luminosity in solar units ($L_\odot$) for the primary (L_1) and secondary stars (L_2) was calculated from the well-known relationship derived from the Stefan-Boltzmann law where:

$$L_{1,2} = (R_{1,2} / R_\odot)^2 (T_{1,2} / T_\odot)^4. \quad (13)$$

Assuming that $T_{eff1} = 5400 \pm 173$ K, $T_{eff2} = 5797 \pm 186$ K, and $T_\odot = 5772$ K, then the stellar luminosities ($L_\odot$) for the primary and secondary are $L_1 = 0.88 \pm 0.11$ and $L_2 = 0.61 \pm 0.08$, respectively. The stellar mass and radius of the primary star closely matches that expected from a stand-alone late

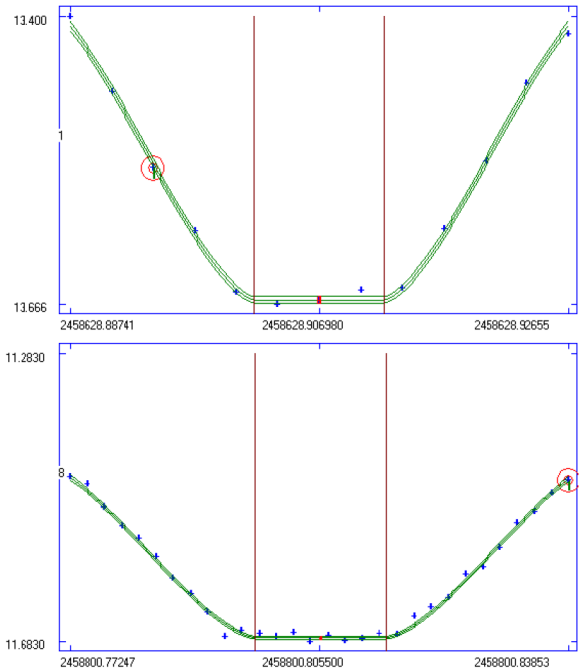

Figure 7. Total eclipse of NSVS 5374825 during Min I (top) and total eclipse of GR Psc during Min II (bottom) as determined using MAVKA. Mean eclipse duration for NSVS 5374825 was estimated to be 15.6 ± 0.8 min whereas the eclipse duration for GR Psc was longer (20.3 ± 0.4 min).

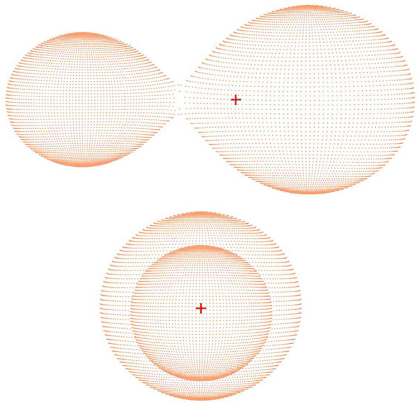

Figure 8. Spatial models of NSVS 5374825 illustrating (bottom) transit of the secondary star across the primary star face at Min II (φ = 0.5) and (top) the shallow contact (f = 0.1) between both stars.

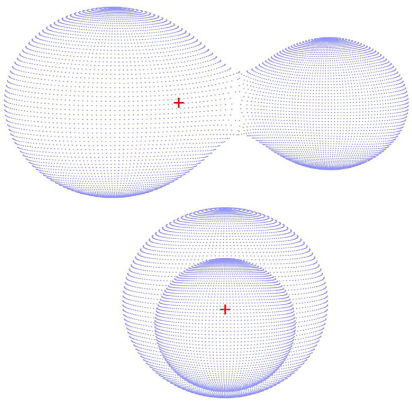

Figure 9. Spatial models of GR Psc showing (bottom) transit of the secondary star at Min I (φ = 0) and (top) the moderate contact (f = 0.43) between both stars.

Table 8. Preliminary stellar parameters for NSVS 5374825 using the mean photometric mass ratio ($q_{ptm} = m_2 / m_1$) from the Roche model fits of LC data (2019) and the estimated mass from four empirical Mass-Period relationships.

Parameter	*Primary*	*Secondary*
Mass ($M_\odot$)	1.12 ± 0.05	0.54 ± 0.02
Radius ($R_\odot$)	1.07 ± 0.01	0.77 ± 0.01
a ($R_\odot$)	2.42 ± 0.02	2.42 ± 0.02
Luminosity ($L_\odot$)	0.88 ± 0.11	0.61 ± 0.08
M_{bol}	4.89 ± 0.14	5.30 ± 0.14
Log (g)	4.43 ± 0.02	4.40 ± 0.02

Table 9. Preliminary stellar parameters for GR Psc using the mean photometric mass ratio ($q_{ptm} = m_2 / m_1$) from the Roche model fits (2019) and the estimated mass from four empirical Mass-Period relationships.

Parameter	*Primary*	*Secondary*
Mass ($M_\odot$)	1.57 ± 0.07	0.68 ± 0.03
Radius ($R_\odot$)	1.56 ± 0.02	1.07 ± 0.01
a ($R_\odot$)	3.45 ± 0.04	3.45 ± 0.04
Luminosity ($L_\odot$)	4.43 ± 0.54	2.02 ± 0.25
M_{bol}	3.13 ± 0.13	3.99 ± 0.13
Log (g)	4.25 ± 0.02	4.22 ± 0.02

G-type main sequence star. However, the secondary star in NSVS 5374825 is considerably more luminous (0.60 vs. 0.14 $L_\odot$) than a field star (K7V) with the same mass ($M_\odot = 0.53$) and a corresponding smaller size ($R_\odot \approx 0.56$).

Based on parallax data in Gaia EDR3 (Gaia Collaboration *et al.* 2021; Lindegren *et al.* 2021), this system can be found at a distance of 475.8 ± 2.9 pc. By comparison, a value derived using the distance modulus equation corrected for interstellar extinction ($A_V = 0.142 \pm 0.0059$) places NSVS 5374825 slightly farther (485.7 ± 36.6 pc) away but within measurement uncertainty. Other values derived herein and necessary to perform this calculation include $V_{max} = 13.01 \pm 0.01$ (Simbad V-mag = 13.03), bolometric correction (BC = –0.11) derived from Pecaut and Mamajek (2013), and the absolute V-magnitude ($M_V = 4.51 \pm 0.22$) from the combined luminosity (4.40 ± 0.22).

3.5.2. GR Psc

The same approach described above for NSVS 5374825 was used to estimate the primary star mass for GR Psc (Table 9) but this time for a putative F1V-F5V system ($T_{eff1} \sim 6700$ K). The mass-period empirical relationships (Equations 7–10) lead to a mean value of 1.57 ± 0.07 $M_\odot$ for the primary star. This is similar to that expected from a single early F-type star. The secondary mass (0.68 ± 0.03 $M_\odot$) and total mass (2.25 ± 0.08 $M_\odot$) of GR Psc were derived from the mean photometric mass ratio (0.432 ± 0.001). If the secondary was a single main sequence star with a similar mass (early K-type) it would probably be much smaller ($R\odot \sim 0.75$), cooler ($T_{eff} \sim 4490$ K), and far less luminous ($L_\odot \sim 0.42$). The semi-major axis, a($R_\odot$) = 3.45 ± 0.04, was calculated from Equation 11 while the effective radius of each Roche lobe (r_L) was calculated according to Equation 12 from which values for r_1 (0.4530 ± 0.0001) and r_2 (0.3091 ± 0.0001) were determined for the primary and secondary stars, respectively. The radii in solar units for both binary components were calculated such that $R_1 = 1.56 \pm 0.02$ $R_\odot$ and $R_2 = 1.07 \pm 0.01$ $R_\odot$. Luminosity in solar units ($L_\odot$) for the primary (L_1) and secondary stars (L_2) was calculated according to Equation 13. Assuming that $T_{eff1} = 6700 \pm 200$ K, $T_{eff2} = 6665 \pm 199$ K, and $T_\odot = 5772$ K, then the stellar luminosities for the primary and secondary are $L_1 = 4.43 \pm 0.54$ and $L_2 = 2.02 \pm 0.25$, respectively. This study and the investigation by Michaels (2020) share very similar values for stellar mass, radius, and semi-major axis. Higher values for stellar luminosity and bolometric magnitude reported in Table 6 from Michaels (2020) are largely attributed to differences in the adopted T_{eff1} values (6811 vs. 6700 K).

This system is estimated to be 555.6 ± 10.3 pc away using the parallax-derived distances reported in Gaia EDR3 (Gaia Collaboration *et al.* 2021). A value independently derived from the distance modulus equation using data generated herein ($V_{max} = 11.06 \pm 0.01$ (Simbad $V_{mag} = 11.06$), $A_V = 0.224 \pm 0.005$, BC = –0.038 and $M_V = 2.76 \pm 0.14$) places GR Psc considerably closer (431.4 ± 29.2~pc).

4. Conclusions

New times of minimum were determined for both NSVS 5374825 and GR Psc based on precise time-series CCD-derived LC data acquired at DBO. These along with other published values and those extracted from the SuperWASP Survey (Butters *et al.* 2010) led to an updated linear ephemeris for each system. Potential changes in orbital period were assessed using differences between observed and predicted eclipse timings. A quadratic relationship was established between the residuals and epoch for both NSVS 5374825 and GR Psc. The orbital period for NSVS 5374825 appeared to be increasing ($0.0185 \cdot y^{-1}$) over a 15 year timespan (2004–2019) while GR Psc was slowly decreasing at a rate of $-0.0126\,s \cdot y^{-1}$. Both systems will require many more years of eclipse timing data to further substantiate any potential change(s) in orbital period. The adopted effective temperatures (T_{eff1}) for NSVS 5374825 (5400 ± 173 K) and GR Psc (6700 ± 200 K) most likely correspond to a G7V-K1V primary star for the former and an F1V-F5V primary for the latter. Both are overcontact systems which exhibit a total eclipse; therefore, the photometric mass ratios for NSVS 5374825 (q = 0.486) and GR Psc (q = 0.432) determined by Roche modeling should prove to be a reliable substitute for mass ratios derived from RV data. Nonetheless, spectroscopic studies (RV and classification spectra) will be required to unequivocally determine a mass ratio, total mass, and spectral class for both systems.

5. Acknowledgements

This research has made use of the SIMBAD database operated at Centre de Données astronomiques de Strasbourg, France. Time-of-minima data tabulated in the Variable Star Section of Czech Astronomical Society (B.R.N.O.) website proved invaluable to the assessment of potential secular changes in orbital period. In addition, the Northern Sky Variability Survey previously hosted by the Los Alamos National Laboratory, the All Sky Automated Survey Catalogue of Variable Stars (http://www.astrouw.edu.pl/asas/?page=acvs), the Catalina Sky

Survey (http://nesssi.cacr.caltech.edu\\/DataRelease/), and the ASAS-SN Variable Stars Database (https://asas-sn.osu.edu/variables) were mined for essential information. This work has made use of data from the European Space Agency (ESA) mission *Gaia* (https://www.cosmos.esa.int/gaia), processed by the *Gaia* Data Processing and Analysis Consortium (DPAC; https://www.cosmos.esa.int/web/gaia/dpac/consortium). Funding for the DPAC has been provided by national institutions, in particular the institutions participating in the *Gaia* Multilateral Agreement. This paper makes use of data from the first public release of the WASP data as provided by the WASP consortium and services at the NASA Exoplanet Archive, which is operated by the California Institute of Technology, under contract with the National Aeronautics and Space Administration under the Exoplanet Exploration Program. The use of public data from LAMOST is also acknowledged. Guoshoujing Telescope (the Large Sky Area Multi-Object Fiber Spectroscopic Telescope LAMOST) is a National Major Scientific Project built by the Chinese Academy of Sciences. Funding for the project has been provided by the National Development and Reform Commission. LAMOST is operated and managed by the National Astronomical Observatories, Chinese Academy of Sciences. Many thanks to the anonymous referee and Editor Morrison for valuable commentary and suggested changes to improve this paper.

References

Akerlof, C., *et al.* 2000, *Astron. J.*, **119**, 1901.
Alton, K. B. 2019, *J. Amer. Assoc. Var. Star Obs.*, **47**, 7.
Alton, K. B., and Nelson, R. H. 2018, *Mon. Not. Roy. Astron. Soc.*, **479**, 3197.
Alton, K. B., Nelson, R. H., and Stępień, K. 2020, *J. Astrophys. Astron.*, **41**, 26.
Andrych, K. D. 2017, *Odessa Astron. Publ.*, **30**, 57.
Andrych, K. D. and Andronov, I.L. 2019, *Open Eur. J. Var. Stars*, **197**, 65.
Andrych, K. D., Andronov, I. L., and Chinarova, L. L. 2020, *J. Phys. Studies*, **24**, 1902.
Banfi, M., *et al.* 2012, *Inf. Bull. Var. Stars*, No. 6033, 1.
Berry, R., and Burnell, J. 2005 *The Handbook of Astronomical Image Processing*, 2nd ed., Willmann-Bell, Richmond, VA.
Binnendijk, L. 1970, *Vistas Astron.*, **12**, 217.
Bradstreet, D. H. 2005, in *The Society for Astronomical Sciences 24th Annual Symposium on Telescope Science*, Society for Astronomical Sciences, Rancho Cucamonga, CA, 23.
Bradstreet, D. H., and Steelman, D. P. 2004, Binary Maker 3, Contact Software (http://www.binarymaker.com).
Butters, O. W., *et al.* 2010, *Astron. Astrophys.*, **520**, L10.
Diethelm, R. 2011, *Inf. Bull. Var. Stars*, No. 5960, 1.
Diethelm, R. 2012, *Inf. Bull. Var. Stars*, No. 6011, 1.
Drake, A. J., *et al.* 2014, *Astrophys. J., Suppl. Ser.*, **213**, 9.
Eggleton, P. P. 1983, *Astrophys. J.*, **268**, 368.
Gaia Collaboration, *et al.* 2016, *Astron. Astrophys.*, **595A**, 1.
Gaia Collaboration, *et al.* 2018, *Astron. Astrophys.*, **616A**, 1.
Gaia Collaboration, *et al.* 2021, *Astron. Astrophys.*, **649A**, 1.
Gazeas, K. D. 2009, *Commun. Asteroseismology*, **159**, 129.
Gazeas, K., and Stępień, K. 2008, *Mon. Not. Roy. Astron. Soc.*, **390**, 1577.
Gettel, S. J., Geske, M. T., and McKay, T. A. 2006, *Astron. J.*, **131**, 621.
Henden, A. A., Levine, S. E., Terrell, D., Smith, T. C., and Welch, D. L. 2011, *Bull. Amer. Astron. Soc.*, **43**.
Henden, A. A., Terrell, D., Welch, D., and Smith, T. C. 2010, *Bull. Amer. Astron. Soc.*, **42**, 515.
Henden, A. A., Welch, D. L., Terrell, D., and Levine, S. E. 2009, *Bull. Amer. Astron. Soc.*, **41**, 669.
Hoffman, D. I., Harrison, T. E., and McNamara, B. J. 2009, *Astron. J.*, **138**, 466.
Houdashelt, M. L., Bell, R. A., and Sweigart, A. V. 2000, *Astron. J.*, **119**, 1448.
Hubscher, J., and Lehmann, P. B. 2013, *Inf. Bull. Var. Stars*, No. 6070, 1.
Jayasinghe, T., *et al.* 2018, *Mon. Not. Roy. Astron. Soc.*, **477**, 3145.
Kafka, S. 2021, Observations from the AAVSO International Database (https://www.aavso.org/data-download).
Kallrath, J., and Milone, E. F. 1999, *Eclipsing Binary Stars: Modeling and Analysis*, Springer, New York.
Kurucz, R. L. 2002, *Baltic Astron.*, **11**, 101.
Latković, O., Čeki, A. and Lazarević, S. 2021, *Astrophys. J., Suppl. Ser.*, **254**, 10.
Li, K., *et al.* 2019, *Res. Astron. Astrophys.*, **19**, 147.
Lindegren, L., *et al.* 2021, *Astron. Astrophys.*, **649A**, 2.
Liu, L. 2021, *Publ. Astron. Soc. Pacific*, **133**, 084202.
Lucy, L. B. 1967, *Z. Astrophys.*, **65**, 89.
Martignoni, M. 2006, *Inf. Bull. Var. Stars*, No. 5700, 1.
Michaels, E. J. 2020, *J. Amer. Assoc. Var. Star Obs.*, **48**, 193.
Minor Planet Observer. 2010, MPO Software Suite (http://www.minorplanetobserver.com), BDW Publishing, Colorado Springs.
Nagai, K. 2012, *Bull. Var. Star Obs. League Japan*, No. 53, 1.
Nagai, K. 2014, *Bull. Var. Star Obs. League Japan*, No. 56, 1.
Nagai, K. 2020, *Bull. Var. Star Obs. League Japan*, No. 67, 1.
Nelson, R. H. 2009, WDwint56a: Astronomy Software by Bob Nelson (https://www.variablestarssouth.org/bob-nelson/).
O'Connell, D. J. K. 1951, *Publ. Riverview Coll. Obs.*, **2**, 85.
Özavcı, I., *et al.* 2019, *Open Eur. J. Var. Stars*, **203**, 1.
Pecaut, M. J,. and Mamajek, E. E. 2013, *Astrophys. J., Suppl. Ser.*, **208**, 9.
Pojmanski, G., Pilecki, B., and Szczygiel, D. 2005, *Acta Astron.*, **55**, 275.
Prša, A., and Zwitter, T. 2005, *Astrophys. J.*, **628**, 426.
Qian, S. 2001, *Mon. Not. Roy. Astron. Soc.*, **328**, 635.
Qian, S. 2003, *Mon. Not. Roy. Astron. Soc.*, **342**, 1260.
Ruciński, S. M. 1969, *Acta Astron.*, **19**, 245.
Samolyk, G. 2015, *J. Amer. Assoc. Var. Star Obs.*, **43**, 77.
Samolyk, G. 2017, *J. Amer. Assoc. Var. Star Obs.*, **45**, 121.
Samolyk, G. 2018, *J. Amer. Assoc. Var. Star Obs.*, **46**, 184.
Schlafly, E. F., and Finkbeiner, D. P. 2011, *Astrophys. J.*, **737**, 103.
Smith, T. C., Henden, A. A., and Starkey, D. R. 2011, in *The Society for Astronomical Sciences 30th Annual Symposium on Telescope Science*, Society for Astronomical Sciences, Rancho Cucamonga, CA, 121.

Software Bisque. 2019, The Sky X professional edition 10.5.0 (https://www.bisque.com).
Terrell, D. 2022, *Galaxies*, **10**, 8.
Terrell, D., Gross, J., and Cooney, W. R. 2012, *Astron. J.*, **143**, 99.
Terrell, D., and Wilson, R. E. 2005, *Astrophys. Space Sci.*, **296**, 221.
Van Hamme, W. 1993, *Astron. J.*, **106**, 2096.
Wang, R., *et al.* 2019, *Publ. Astron. Soc. Pacific*, **131**, 024505.
Wilson, R. E. 1979, *Astrophys. J.*, **234**, 1054.
Wilson, R. E. 1990, *Astrophys. J.*, **356**, 613.
Wilson, R. E. and Devinney, E.J. 1971, *Astrophys. J.*, **166**, 605.
Woźniak, P. R., *et al.* 2004, *Astron. J.*, **127**, 2436.
Zhao, G., Zhao, Y.-H., Chu, Y.-Q., Jing, Y.-P., and Deng, L.-C. 2012, *Res. Astron. Astrophys.*, **12**, 723.